Progress In Electromagnetics Research, Vol. 137, 621–642, 2013

A NOVEL THREE-STEP IMAGE FORMATION SCHEME FOR UNIFIED FOCUSING ON SPACEBORNE SAR DATA

Wei Yang, Jie Chen*, Hongceng Zeng, Jian Zhou, Pengbo Wang, and Chunsheng Li

School of Electronic and Information Engineering, Beihang University, Beijing, China

Abstract—Current advanced spaceborne synthetic aperture radar (SAR) systems may operate at multiple imaging modes, including conventional modes as stripmap, ScanSAR and spotlight, as well as the state-of-the-art SAR modes, e.g., sliding spotlight, TOPS (Terrain Observation by Progressive Scans) and inverse TOPS etc. A novel image formation scheme for unified processing spaceborne SAR data was proposed, which significantly simplified complexity of SAR processor sub-system. The unified-model-coefficient (UMC) was defined for modeling all SAR modes by means of analyzing both imaging geometry and time-frequency diagram corresponding to each imaging mode, respectively. The unified mathematical formula for modeling all SAR modes echo signal was derived as a function of UMC. Consequently, a unified image formation scheme for accurately focusing spaceborne SAR data in an arbitrary mode was proposed, which integrates all of SAR image formation procedures into a standard three-step processing framework, namely, de-rotation, data focusing and re-sampling, which evidently improve efficiency and robustness of data processing sub-system. Computer simulation experiment results verify the effectiveness of the proposed scheme.

1. INTRODUCTION

Spaceborne Synthetic Aperture Radar (SAR) plays more and more significant roles in both civil remote sensing and military surveillance applications [1–5]. In order to satisfy the requirements from recent remote sensing applications, most currently advanced spaceborne SAR

Received 23 December 2012, Accepted 4 March 2013, Scheduled 7 March 2013

* Corresponding author: Jie Chen (chenjie@buaa.edu.cn).

sensors have multiple imaging modes to implement high-resolution and wide-swath Earth observation capability, which may operate at both conventional SAR modes, including stripmap mode, ScanSAR mode as well as spotlight mode, and state-of-the-art SAR modes, including sliding spotlight mode, TOPS (Terrain Observation by Progressive Scans) mode and inverse TOPS mode et al. [6–9].

Current SAR processor should employ various image formation algorithms for focusing different imaging modes SAR data. As for conventional modes, several classical image formation algorithms were proposed, including SPEACAN algorithm [10], range Doppler algorithm (RDA) [11], chirp scaling algorithm (CSA) [12], extended chirp scaling algorithm (ECSA)[13], frequency scaling algorithm (FSA) [14], polar format algorithm (PFA) [15], and wavenumber domain algorithm (WDA) [16], as well as their modified algorithms [17–20]. SPEACAN algorithm has high efficiency for focusing ScanSAR data, but it cannot be applied to process other modes of SAR data, due to highly approximate assumptions. RDA is only suitable for focusing the low/moderate-resolution SAR data, e.g., stripmap data, for low efficiency and accuracy in processing SAR data with large range cell migration (RCM). CSA performs well in both efficiency and accuracy performance but only for processing stripmap data, since it cannot deal with azimuth spectral folding in spotlight, sliding spotlight, TOPS and Inverse TOPS data. ECSA is only applied in processing ScanSAR data, because of neglecting the range-dependent property of second range compression (SRC). FSA, PFA and WDA are proposed mainly for processing spotlight data, which cannot be utilized for focusing SAR data in wide-swath modes, e.g., TOPS, Inverse TOPS and ScanSAR.

For the state-of-the-art imaging modes, several specified imaging formation algorithms were recently developed [21–25]. A two-step image formation algorithm was proposed for processing spotlight and sliding spotlight SAR data [21]. Moreover, baseband-azimuth-scaling (BAS) algorithm [22] and extended three-step algorithm (ETSA) [23] were developed for focusing both TOPS and sliding spotlight SAR data. However, both BAS and ETSA cannot be utilized to process stripmap, ScanSAR and spotlight SAR data. Meanwhile, the two-step image formation algorithm is not feasible for processing stripmap, ScanSAR and TOPS SAR data. Therefore, no image formation algorithms can focus all modes spaceborne SAR data. As a result, different imaging formation algorithms have to be developed in SAR processor to accurately focus multiple modes SAR data, which leads to degradations on accuracy and efficiency of data processing at ground-segment of SAR satellite.

In order to solve this problem, a unified-model-coefficient (UMC)

was firstly defined in this paper, for uniformly modeling all SAR modes according to their UMC value. As a result, a unified image formation scheme was proposed, which synergizes all modes SAR processing procedures into a standard three-step processing framework, namely, de-rotation, data focusing and re-sampling processing steps. Different from the traditional image formation schemes, which have to employ different image formation algorithms for focusing the specified mode of SAR data, the proposed scheme is capable to focus the multiple modes SAR data through only one unified three-step procedure, which means all modes SAR data can be automatically identified according to its UMC value calculated by using auxiliary data from SAR raw data records. Therefore, efficiency and robustness of ground-processing system of SAR satellite is evidently improved.

In Section 2, the UMC is defined based on spaceborne SAR observation geometry. Moreover, the mathematical model for describing relationship between UMC and the imaging modes is also investigated in details. In Section 3, a novel data processing scheme is proposed based on UMC. Section 4 demonstrates the simulation results by implementing the unified three-step image formation scheme for data processing. Finally, conclusions are presented in Section 5.

2. UNIFIED GEOMETRY FOR SPACEBORNE SAR

A unified geometry for spaceborne SAR imaging modes is shown in Figure 1, where unified-model-coefficient (UMC) γ is defined by

$$\gamma = \frac{R_{rs}}{R_{rg}} \tag{1}$$

where R_{rs} represents the minimum distance from rotation point to SAR sensor, and R_{rg} denotes the minimum distance from rotation point to ground scene [24], and subscripts r, s, and g are referred to as rotation point, SAR sensor, and ground target, respectively.

SAR Doppler history characteristics are fundamentals of unified data processing. On basis of defining UMC parameter, Doppler history characteristic of each SAR mode can be analyzed according to its UMC value by introducing Doppler time-frequency diagram (TFD) (see Figures 2–7), respectively. A_1, A_2 and A_3 represent three targets located along azimuth direction, namely, A_1 and A_3 denote the azimuth corner point targets, while A_2 accounts for the center point target in the ground scene. And, X_L and X_R represent the regions with insufficient accumulation of illumination time. Moreover, v, λ, ω_φ and f_{prf} are referred to as satellite velocity, radar wavelength, azimuth antenna-beam angular velocity and pulse repetition frequency (PRF).

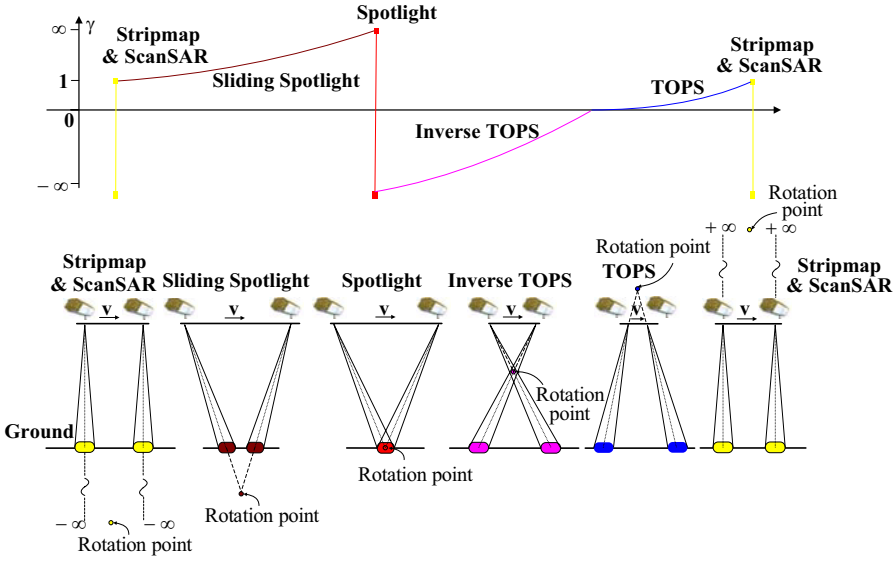

Figure 1. Unified geometry for spaceborne SAR imaging modes.

Furthermore, k_r and k_ω represent Doppler rate and antenna sweep rate [6], respectively, which can be written as

$$k_\omega = \frac{2v^2}{\lambda R_{rs}} \tag{2a}$$

$$k_r = \frac{2v^2}{\lambda \left(R_{rs} - R_{rg}\right)} \tag{2b}$$

$B_{3\,\mathrm{dB}}$ represents 3 dB Doppler bandwidth. And, f_{prf} should be larger than $B_{3\,\mathrm{dB}}$ for satisfying the Nyquist sampling theorem, which is the precondition for SAR data processing.

$B_{\max}$ stands for the maximum Doppler bandwidth of each target that defines the best azimuth resolution. $B_{\max}$ can be written as

$$B_{\max} = B_{3\,\mathrm{dB}} \cdot \gamma \tag{3}$$

B_{tar} denotes the Doppler bandwidth for each point target in reality, which defines the real azimuth resolution. B_{tar} is given by

$$B_{tar} = k_r T_{tar} \tag{4}$$

where T_{tar} refers to target illumination time.

B_{total} is referred to as the total Doppler bandwidth [22], consisting of $B_{3\,\mathrm{dB}}$ and B_{steer}, which is given by

$$B_{total} = B_{3\,\mathrm{dB}} + B_{steer} \tag{5}$$

B_{steer} denotes the Doppler bandwidth resulting from azimuth antenna-beam steering, which can be written by

$$B_{steer} = |k_\omega| T_{scene} \tag{6}$$

where T_{scene} represents scene illumination time.

2.1. Stripmap Mode

As for stripmap mode, azimuth antenna-beam is steered about infinity, namely, rotation point locates at infinite (see Figure 2). Therefore, azimuth antenna-beam points along a fixed direction, which means B_{steer} is equal to zero. Moreover, target illumination time T_{tar} is calculated by $B_{3\,\mathrm{dB}}/k_r$, considering $\gamma = 1$ in stripmap mode, $B_{total} = B_{\max} = B_{tar}$ is deduced according to the Equations (3)–(5).

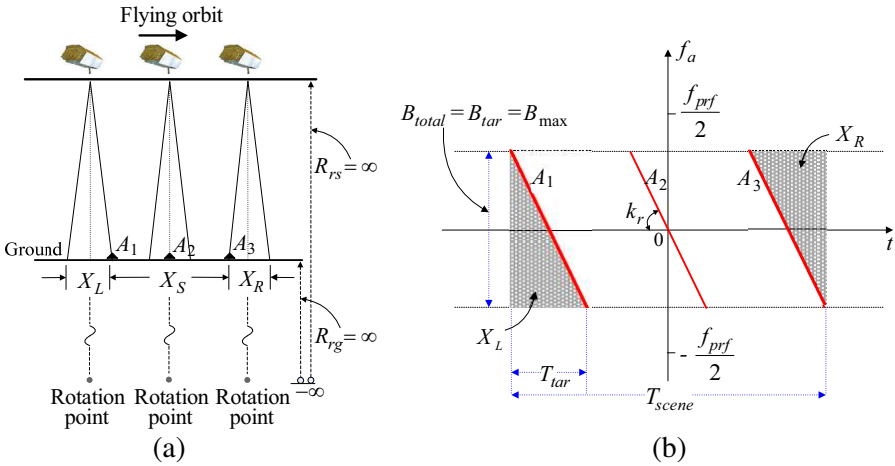

Figure 2. Stripmap mode. (a) Imaging geometry, (b) time-frequency diagram.

2.2. Sliding Spotlight Mode

As shown in Figure 3, azimuth antenna-beam is steered about a rotation point located underground, and the steering direction is from forth to back in sliding spotlight mode. Accordingly, antenna-beam footprint move at a lower velocity, leading to larger target illumination time and improved azimuth resolution with respect to that of stripmap case. Because of antenna-beam steering, an extension of Doppler bandwidth B_{steer} is appearance, resulting in azimuth spectral folding

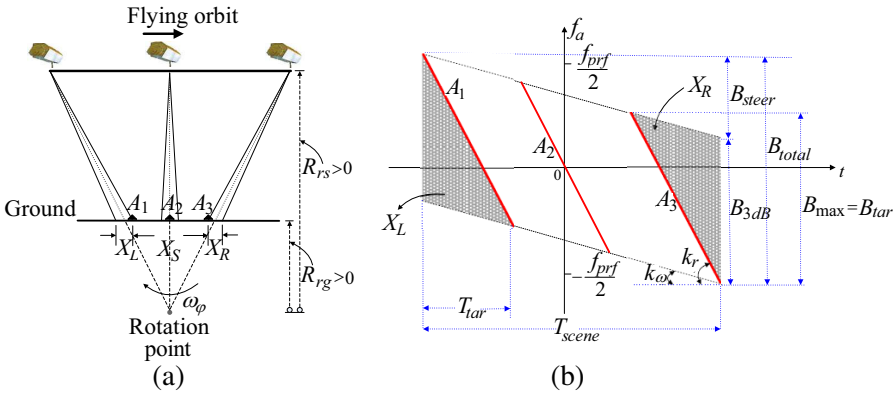

Figure 3. Sliding spotlight mode. (a) Imaging geometry, (b) time-frequency diagram.

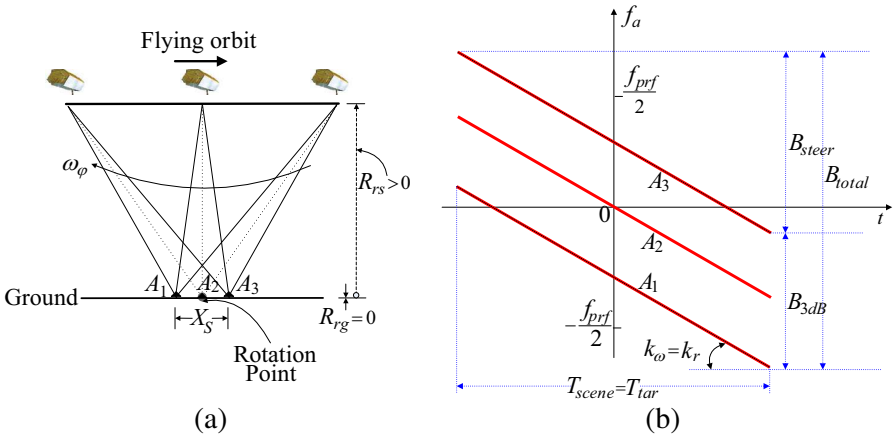

Figure 4. Spotlight mode. (a) Imaging geometry, (b) time-frequency diagram.

phenomenon, namely, B_{total} is larger than f_{prf}. Furthermore, $\gamma > 1$ in sliding spotlight mode according to the imaging geometry, and $B_{\max}$ is equal to B_{tar} on basis of TFD.

2.3. Spotlight Mode

Rotation point is located on the surface of scene in spotlight mode (see Figure 4), and the steering direction is the same as the sliding spotlight case. Therefore, antenna-beam footprint keeps stationary on

ground, and all the targets are illuminated at the same time, resulting in $T_{tar} = T_{scene}$. For a determined steering angle range, spotlight mode provides the best azimuth resolution. Theoretically speaking, steering angle range is from $-\pi$ to π, which means T_{tar} can be diverges to infinity and $B_{\max}$ can be diverges limit value. Actually, T_{tar} is limited according to the required azimuth resolution, so the real azimuth resolution is dependent on B_{tar}. As a result, γ diverges to infinity, and $B_{\max}$ is larger than B_{tar} in spotlight mode, which is different from other SAR modes.

2.4. Inverse TOPS Mode

In inverse TOPS mode, rotation point is located between ground and sensor, so γ is negative according to the definition in Equation (1). Azimuth antenna-beam is steered with the same direction as sliding spotlight and spotlight modes, while the antenna sweep rate k_ω is larger than Doppler rate k_r, which is the particular characteristic of inverse TOPS mode. Wide-Swath image can be acquired in inverse TOPS mode, but a larger steering angle is required when compared with TOPS mode.

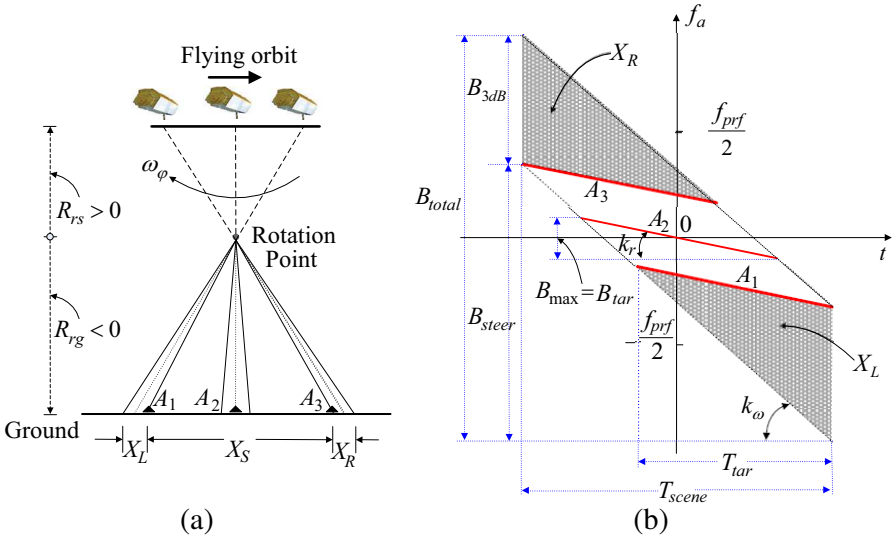

Figure 5. Inverse TOPS mode. (a) Imaging geometry, (b) time-frequency diagram.

2.5. TOPS Mode

As for TOPS mode, rotation point is located above the SAR sensor, which is shown in Figure 6. It employs a very simple counter-clockwise steering of azimuth antenna beam, namely, the opposite direction comparing to inverse TOPS, spotlight as well as sliding spotlight modes, so k_ω is negative only in TOPS mode. The azimuth resolution reduction is caused by a shorter target illumination time, and B_{tar} is smaller than f_{prf}. However, the total Doppler bandwidth B_{total} might span over several f_{prf} intervals for antenna-beam steering. Therefore, the azimuth frequency aliasing is also happened in TOPS mode.

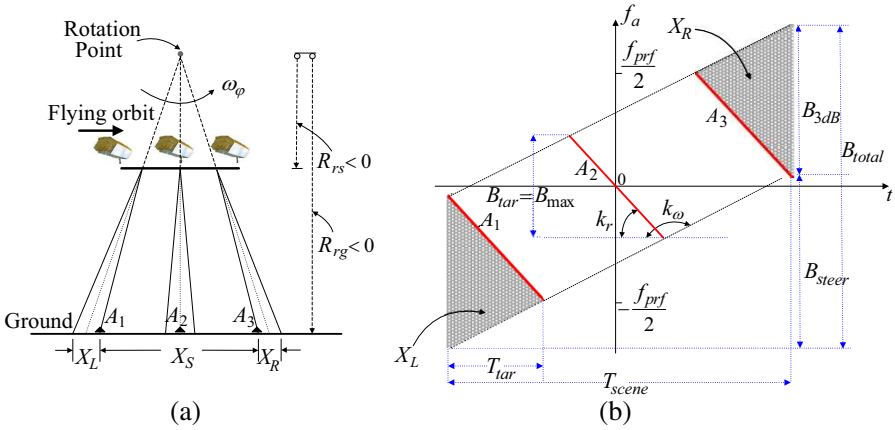

Figure 6. TOPS mode. (a) Imaging geometry, (b) Time-frequency diagram.

2.6. ScanSAR Mode

As shown in Figure 7, azimuth antenna-beam point is fixed in ScanSAR mode, which is similar with stripmap mode. However, a larger illumination area in cross-track direction is obtained by switching the elevation beam. Therefore, every target is illuminated with only a small portion of the antenna pattern, and azimuth resolution is reduced comparing with stripmap mode. ScanSAR is a sub-aperture imaging mode, and all the targets have accumulated the same illumination time, resulting in $T_{tar} = T_{scene}$ and $B_{total} = B_{3\,\mathrm{dB}}$.

2.7. Summary

Considering all SAR imaging modes, several important parameters are compared and summarized in Table 1.

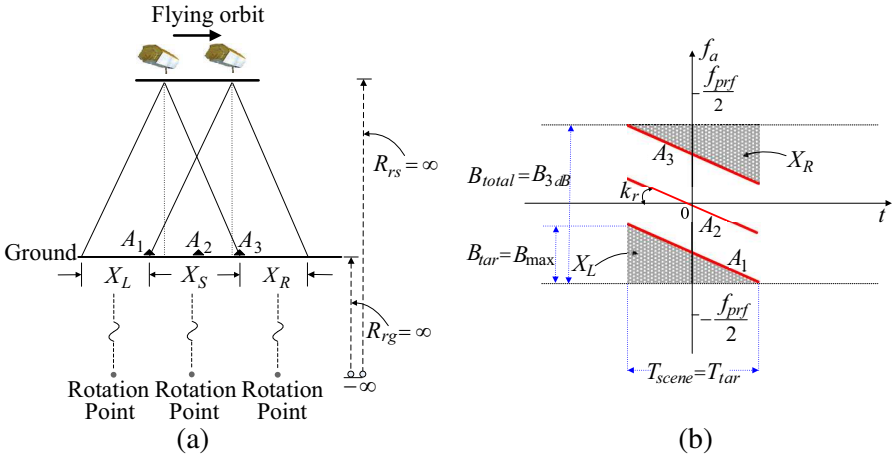

Figure 7. ScanSAR mode. (a) Imaging geometry, (b) time-frequency diagram.

Table 1. Parameters of different SAR imaging modes.

	γ	k_ω	B_{tar}	T_{tar}
Stripmap	1	0	$B_{\max}=B_{tar}=B_{3\,\mathrm{dB}}$	$T_{tar}<T_{scene}$
Sliding Spotlight	>1	$k_r>k_\omega>0$	$B_{\max}=B_{tar}>B_{3\,\mathrm{dB}}$	$T_{tar}<T_{scene}$
Spotlight	∞	$k_r=k_\omega>0$	$B_{\max}>B_{tar}>B_{3\,\mathrm{dB}}$	$T_{tar}=T_{scene}$
Inverse TOPS	<0	$k_\omega>k_r>0$	$B_{\max}=B_{tar}$	$T_{tar}<T_{scene}$
TOPS	$0\sim1$	$0>k_\omega$	$B_{\max}=B_{tar}<B_{3\,\mathrm{dB}}$	$T_{tar}<T_{scene}$
ScanSAR	1	0	$B_{\max}=B_{3\,\mathrm{dB}}>B_{tar}$	$T_{tar}=T_{scene}$

Based on the analysis above, arbitrary SAR imaging mode is satisfied the Equations (4) and (5). However, all the above analysis is only consider the conference slant range, so it is necessary to study the characteristic of UMC along slant range.

Actually, the significant discrimination among SAR imaging modes is the steering rules of azimuth antenna-beam, which affect the azimuth antenna pattern (AAP) modulation shown as follow

$$W_a(t)=\mathrm{sinc}^2\left(\frac{L}{\lambda}\cdot\left(\frac{vt}{r}-\omega_\varphi t\right)\right) \tag{7}$$

where L represents the length of azimuth antenna, and r represents slant range.

Since UMC can indicate both steering direction and angular velocity ω_φ of azimuth antenna-beam, azimuth antenna pattern can

be rewritten as a function of UMC. Considering $\omega_\varphi = v/R_{rs}$ is independent on slant range, AAP is given by

$$W_a(t) = \mathrm{sinc}^2\left(\frac{L}{\lambda}\cdot\frac{vt}{r}\cdot\frac{R_{rs}-r}{R_{rs}}\right) = \mathrm{sinc}^2\left(\frac{L}{\lambda}\cdot\frac{vt}{r}\cdot\frac{1}{\gamma(r)}\right) \quad (8)$$

where the modified UMC, i.e., $\gamma(r)$, can be given by

$$\gamma(r) = \frac{R_{rs}}{R_{rs}-r} \quad (9)$$

$\gamma(r)$ slightly varies with r, leading to azimuth resolution $\rho_a(r)$ changes with r, which was neglected in [6–10, 18–22]. Moreover, this phenomenon was considered in the following analysis, and some significant conclusions were deduced based on the modified UMC.

3. UNIFIED SAR IMAGE FORMATION SCHEME

3.1. Unified Mathematic Model

The unified mathematical model of spaceborne SAR modes is given by

$$\begin{aligned} &S(\tau, t-t_A; r) \\ &= \mathrm{rect}\left(\frac{vt/\gamma(r)-vt_A}{X_{\Delta\theta}}\right)\cdot\mathrm{rect}\left(\frac{t}{T_{scene}}\right)\cdot\mathrm{rect}\left(\frac{vt_A}{X_s}\right)\cdot W_a(t)\cdot W_r(t) \\ &\cdot p\left(\tau-\frac{2r(t;r)}{c}\right)\cdot\exp\left\{-j\pi b\left(\tau-\frac{2r(t;r)}{c}\right)^2\right\}\cdot\exp\left\{-j\frac{4\pi r(t;r)}{\lambda}\right\} \end{aligned} \quad (10)$$

where $\mathrm{rect}(\cdot)$ represents the rectangular window, $W_r(t)$ the range antenna pattern, $p(\cdot)$ the envelop of linear frequency modulation signal, b the signal frequency modulation rate, c the speed of light, and τ and t represent range fast time and azimuth slow time, respectively. The slant range history $r(t;r)$ is given by

$$r(t;r) = \sqrt{r^2 + v^2(t-t_A)^2} = r + \Delta r \approx r + \frac{\lambda}{4}k_r(t-t_A)^2 \quad (11)$$

Moreover, the contribution focus on the azimuth signal processing, assuming that range cell migration (RCM) and amplitude factors have been corrected. Then, azimuth signal can be given by

$$\begin{aligned} S_A(t-t_A; t_A, r) \;=\; &\mathrm{rect}\left(\frac{vt/\gamma(r)-vt_A}{X_{\Delta\theta}}\right)\cdot\mathrm{rect}\left(\frac{t}{T_{scene}}\right)\cdot\mathrm{rect}\left(\frac{vt_A}{X_S}\right) \\ &\cdot\exp\left\{-j\pi k_r(t-t_A)^2\right\} \end{aligned} \quad (12)$$

where $X_{\Delta\theta} = \lambda r/L$ is the azimuth antenna footprint.

By applying the stationary phase method, azimuth Doppler spectrum can be written as

$$S_{f_a}(f_a; t_A, r) = \text{rect}\left(-\frac{f_a - k_r(1-\gamma(r))t_A}{B_{3\,\text{dB}}\gamma(r)}\right) \cdot \text{rect}\left(-\frac{f_a - k_r t_A}{k_r T_{scene}}\right) \cdot \text{rect}\left(\frac{vt_A}{X_s}\right) \cdot \exp\left\{j\pi\frac{f_a^2}{k_r} - 2\pi f_a t_A\right\} \quad (13)$$

For full-aperture imaging mode, the first term of Equation (13) defines Doppler history characteristic. As for sub-aperture imaging mode (namely ScanSAR), the second term plays the decisive role. However, whether full-aperture or sub-aperture imaging mode, B_{total} is composed by two parts, i.e., $B_{3\,\text{dB}}$ and B_{steer}. Furthermore, $B_{3\,\text{dB}}$ and B_{steer} are independent with slang range, which means B_{total} is not variant with UMC. And, this is the theoretical fundamentals of the proposed unified three-step image formation scheme for focusing spaceborne SAR data in arbitrary mode.

3.2. Step 1: De-rotation Processing

Because of azimuth antenna beam rotation, the total Doppler bandwidth might span over several f_{prf} intervals. In order to avoid azimuth spectral aliasing, the first step is implemented to compensate B_{steer}, which is named de-rotation operation.

The de-rotation operation involves azimuth signal convolution between the raw signal and the following signal [6]

$$H_{De\text{-}rotation}(t) = \exp\left\{j\pi k_\omega t^2\right\} \quad (14)$$

Then, the convolution result is given by

$$\begin{aligned} S_1(t - t_A; t_A, r) &= S(t - t_A; t_A, r) \otimes_t H_{De\text{-}rotation}(t) \\ &\approx \text{rect}\left[\frac{vt_A}{X_s}\right] \cdot \text{rect}\left[-\frac{t}{\frac{\lambda R_{rs}}{Lv}}\right] \cdot \text{rect}\left[\frac{t - \frac{R_{rs}}{r}t_A}{T_{scene}\left(\frac{r-R_{rs}}{r}\right)}\right] \\ &\quad \cdot \exp\left\{j\pi k_e(r)(t - t_A)^2\right\} \end{aligned} \quad (15)$$

where $k_e(r)$ is given by

$$k_e(r) = \frac{2v^2}{\lambda(R_{rs} - r)} \quad (16)$$

According to the geometry of Figures 2–7, the inequality is given by

$$\left|T_{scene}\left(\frac{r - R_{rs}}{r}\right)\right| > \left|\frac{\lambda R_{rs}}{Lv}\right| \quad (17)$$

So, the second term plays a significant role. And some important conclusions after de-rotation operation are given by mathematic derivation:

(1) The targets located at different azimuth position are totally overlapped after de-rotation, so the azimuth weighting could be implemented following de-rotation operation. Moreover, the signal time width T' in azimuth deduced according to the second term of Equation (15) is give by

$$T' = \frac{\lambda |R_{rs}|}{Lv} \tag{18}$$

(2) After de-rotation operation, the equivalent PRF, referred to as f'_{prf} is given by

$$f'_{prf} = \frac{N |k_\omega|}{f_{prf}} \tag{19}$$

where N is the point number of fast Fourier transform (FFT).

(3) In order to avoid azimuth spectral overlapping, $f'_{prf} > B_{total}$ should be satisfied. So, the zero padding is applied before de-rotation, and N is selected according to the Equation (20).

$$N > f_{prf} \frac{\lambda |R_{rs}|}{Lv} + f_{prf} T = N_0 + N_a \tag{20}$$

where, N_a is the point number of azimuth raw signal and N_0 the point number of zero padding that is independent on slant range r.

(4) After zero padding, the width of time domain T_1 is given as follow

$$T_1 = \frac{N}{f'_{prf}} = \frac{f_{prf}}{|k_\omega|} > \frac{B_{3\,\mathrm{dB}}}{|k_\omega|} = \frac{\lambda |R_{rs}|}{Lv} = T' \tag{21}$$

As shown in Equation (21), T_1 is longer than T'. So, there is no time aliasing after de-rotation operation.

(5) For stripmap and ScanSAR mode, k_ω is zero. That is means the de-operation is not necessary for the processing of stripmap and ScanSAR data.

(6) De-rotation can be implemented by means of complex multiply and FFT, including azimuth de-chirp, azimuth FFT and azimuth re-chirp [21–23].

3.3. Step 2: Data Focusing

Since the folding effect in azimuth frequency domain is overcome after de-rotation operation, any of the image formation algorithm kernel, for example, CSA, WDA, RDA, FSA, et al., can be employed to implement range cell migration correction (RCMC), range compression, second

range compression (SRC), as well as hyperbolic phase remove. Note that, the equivalent PRF should be used, when the data focusing step is implemented.

However, in order to realize both high-resolution and wide-swath, a large azimuth steering angle range is required, which means the targets at azimuth edge are illuminated with a squint angle. So, current squint mode imaging algorithms, e.g., nonlinear CS (NCS) algorithms [25], 2D interpolation algorithm [17], azimuth nonlinear chirp scaling (NLCS) algorithm [20] et al., can be also selected to implement data focusing in Step 2.

Considering the processing efficiency and accuracy, the CSA algorithm kernel is adopted in this paper [12]. And, the phenomenon of high order phase error in 2D frequency and the curved orbit are also taken into account in sliding spotlight mode and spotlight mode [26].

So, according to different data processing requirements, different algorithm kernels can be chosen in unified image formation scheme three-step, which improves the flexibility and robustness of SAR processor.

3.4. Step 3: Re-sampling Processing

Because of de-rotation operation, image aliasing will likely occur in azimuth, if azimuth inverse fast Fourier transform (IFFT) is applied after hyperbolic phase removing. The condition of image aliasing is given by

$$T_1 = \frac{N}{f'_{prf}} = \frac{f_{prf}}{|k_\omega|} < \frac{X_s}{v} = T_{image} \tag{22}$$

where T_{image} is the azimuth time of final image. So, the lower limit of f_{prf} is $|k_\omega|X_s/v$. However, the higher f_{prf} is, the narrower the swath is and the larger N_a is. And, if N_a become larger, data processing efficiency will deteriorate. In order to avoid image aliasing, an innovative re-sampling operation is proposed that could overcome the image aliasing without limitation by Equation (22).

Since the targets located at different azimuth position are overlapped in time domain, and separated in Doppler domain. By using the stationary phase method, the Doppler domain expression of $S_1(t - t_A;\, t_A,\, r)$ is given by

$$S'_{f_a}(f_a; t_A, r) = \mathrm{rect}\left(-\frac{f_a + k_e(r)t_A}{B_{3\,\mathrm{dB}}\gamma(r)}\right) \cdot \mathrm{rect}\left(-\frac{f_a - k_r t_A}{k_r T_{scene}}\right) \cdot \mathrm{rect}\left(\frac{vt_A}{X_s}\right) \cdot \exp\left\{j\pi \frac{f_a^2}{-k_e(r)} - 2\pi f_a t_A\right\} \tag{23}$$

Compared with $S_{f_a}(f_a; t_A, r)$ shown in Equation (13), the Doppler frequency modulation rate is changed from k_r to $-k_e(r)$. However, in focusing operation, k_r is used for azimuth compression. So the residual quadratic phase is shown in (24):

$$\Delta\Phi_1 = -j\pi f_a^2 \left(\frac{1}{k_e(r)} + \frac{1}{k_r}\right) = -j\pi \frac{f_a^2}{k_\omega} \tag{24}$$

Consequently, signal should be multiplied by the following phase function.

$$H_{re\text{-}sampling}(f_a) = \exp\left\{j\pi \frac{f_a^2}{k_\omega}\right\} \cdot \exp\left\{-j\pi \frac{f_a^2}{k_e(r_0)}\right\} \tag{25}$$

where r_0 is the reference slant range. The first exponential term compensate the residual phase caused by de-rotation and the second exponential term introduces the quadratic phase.

In fact, $\Delta\Phi_1$ is independent on slant range, and is compensated by the first exponential term in (25). Moreover, the second exponential term is adopted to finish re-sampling. So signal $S'_{f_a}(f_a; t_A, r)$ is changed to $S''_{f_a}(f_a; t_A, r)$ after multiplying $H_{re\text{-}sampling}(f_a)$.

$$\begin{aligned} S''_{f_a}(f_a; t_A, r) = {} & \text{rect}\left(-\frac{f_a + k_e(r)t_A}{B_{3\,\text{dB}}\gamma(r)}\right) \cdot \text{rect}\left(-\frac{f_a - k_r t_A}{k_r T_{scene}}\right) \cdot \text{rect}\left(\frac{vt_A}{X_s}\right) \\ & \cdot \exp\left\{j\pi \frac{f_a^2}{-k_e(r_0)} - 2\pi f_a t_A\right\} \end{aligned} \tag{26}$$

After IFFT operation, the time-domain expression of the radar signal can be written as

$$\begin{aligned} S_2(t - t_A; t_A, r) = {} & \text{rect}\left[\frac{vt_A}{X_s}\right] \cdot \text{rect}\left[\frac{t - \frac{R_{rs}+r-r_0}{r} t_A}{T_{scene}\left(\frac{r_0 - R_{rs}}{r}\right)}\right] \cdot \text{rect}\left[-\frac{t - \frac{r_0 - r}{R_{rs} - r} t_A}{\frac{\lambda R_{rs}}{Lv}}\right] \\ & \cdot \exp\left\{j\pi k_e(r_0)(t - t_A)^2\right\} \end{aligned} \tag{27}$$

Compare the denominator of the second and the third term,

$$\left|\frac{\lambda R_{rs}}{Lv}\right| = \left|\frac{\lambda r}{Lv} \frac{R_{rs}}{r_0 - R_{rs}} \frac{r_0 - R_{rs}}{r}\right| = \frac{\gamma(r_0) X_{\Delta\theta}}{vT_{scene}} \left|T_{scene}\left(\frac{r_0 - R_{rs}}{r}\right)\right| \tag{28}$$

Because $X_{\Delta\theta} < vT_{scene}/\gamma(r_0)$, the third term in (27) plays a significant role. Therefore, the azimuth time extension ΔT is given by

$$\Delta T = \frac{X_s}{v} \cdot \left|\frac{r_0 - r}{R_{rs} - r}\right| = \frac{X_s}{v} \cdot \left|\frac{\Delta r}{R_{rg} + \Delta r}\right| = \left(\frac{T_{scene}}{\gamma(r)} - \frac{X_{\Delta\theta}}{v}\right) \cdot \left|\frac{\Delta r}{R_{rg} + \Delta r}\right| \tag{29}$$

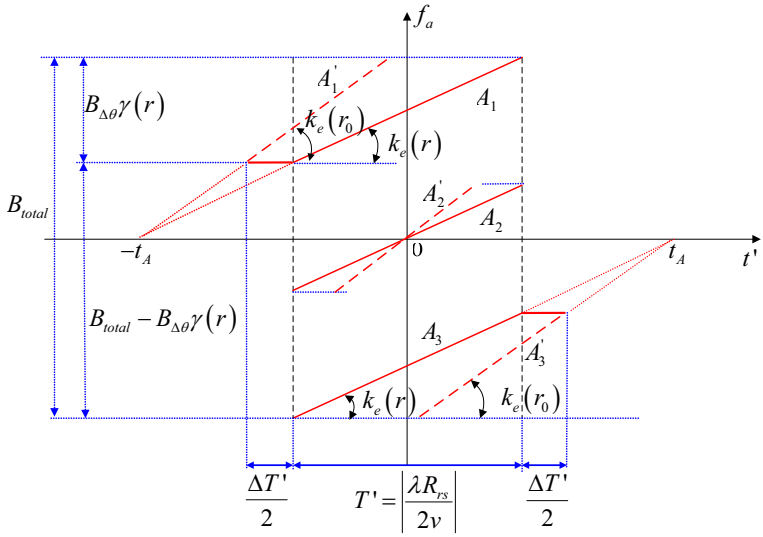

Figure 8. Comparing Doppler history changing of 3 targets in time-frequency diagram before (A_1, A_2 and A_3) and after (A_1', A_2' and A_3') re-sampling.

The same result can be derived by using azimuth time-frequency diagram shown in Figure 8. However, ΔT usually is small enough to be neglected.

Furthermore, the quadric phase is compensated by Equation (30):

$$H(t) = \exp\left\{-j\pi k_e(r_0)\, t^2\right\} \tag{30}$$

Then, the image is obtained by azimuth IFFT.

After re-sampling operation, the re-sampling rate f''_{prf} is given by

$$f''_{prf} = \frac{N\left|k_e(r_0)\right|}{f'_{prf}} = \frac{R_{rs}}{R_{rs}-r_0} f_{prf} = \gamma(r_0)\, f_{prf} \tag{31}$$

Then, azimuth time width T'' can be written as

$$T'' = \frac{N}{f''_{prf}} > \frac{N_a}{f_{prf}\gamma(r_0)} = \frac{T_{scene}}{\gamma(r_0)} \tag{32}$$

According to the unified geometry, the inequality is given by

$$vT_{scene}/\gamma(r_0) = X_{\Delta\theta} + X_s > X_s \tag{33}$$

So, combined the Equations (32) and (33),

$$T'' > \frac{T_{scene}}{\gamma(r_0)} > \frac{X_s}{v} = T_{image} \tag{34}$$

That means the azimuth aliasing of image is overcome.

The flowchart of image formation scheme for unified SAR data processing is shown in Figure 9, and the CS algorithm kernel is adopted to finish data focusing.

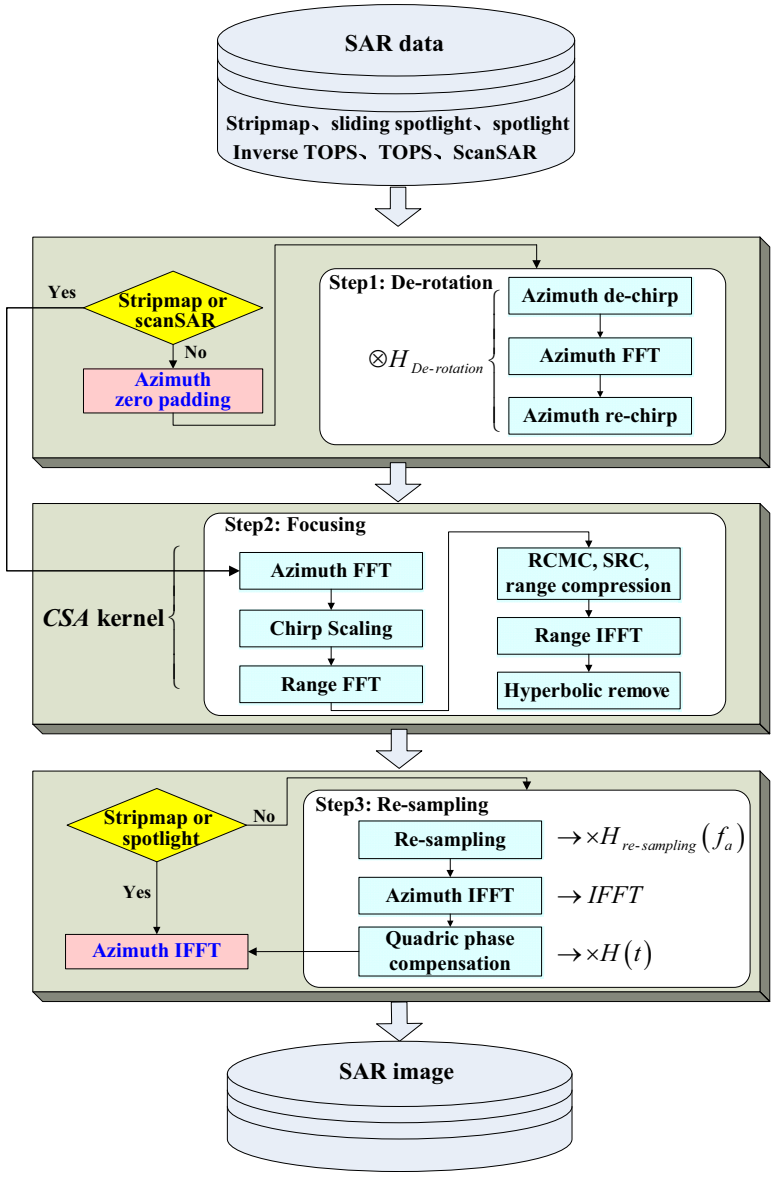

Figure 9. The flowchart of image formation scheme for unified SAR data processing.

4. SIMULATION AND DISCUSSIONS

The numerical simulations were implemented in order to verify the effectiveness of the proposed method. The simulation parameters are listed in Table 2. Assuming 9 point targets were displaced in the scene with constant interval d apart from each other (see Figure 10).

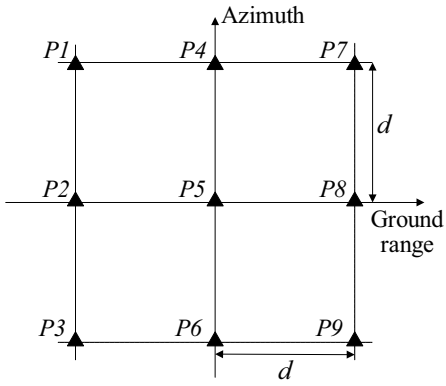

Figure 10. Simulation scene.

Table 2. Simulation parameters.

Parameters	Values
Platform height (km)	514
Wavelength (m)	0.03
Incidence angle (deg)	35
Pulse width (μs)	30
Antenna length (m)	4.784

In order to verify the applicability of unified image formation scheme for processing both the conventional SAR imaging modes and the state-of-the-art imaging modes, and to prove the conclusion that azimuth resolution varies with slant range, special parameters are selected in different imaging mode. To evidently demonstrate the change of azimuth resolution, d is set as the 5000 m, 2000 m, 1000 m, 3000 m, 3000 m and 2000 m in stripmap, sliding spotlight, spotlight, inverse TOPS, TOPS and ScanSAR mode, respectively. Simultaneously, to verify the capability of unified image formation scheme for dealing with the high resolution imaging modes, including spotlight and sliding spotlight mode, and the wide swath imaging

modes, including TOPS, inverse TOPS and ScanSAR mode, the pulse bandwidth is set as 100 MHz, 500 MHz, 1000 MHz, 25 MHz, 20 MHz and 12 MHz in stripmap, sliding spotlight, spotlight, inverse TOPS, TOPS and ScanSAR mode, respectively. According, the sampling rates are 110 MHz, 550 MHz, 1100 MHz, 35 MHz, 30 MHz and 20 MHz.

The simulated data include the radar echoes from a 3×3 point targets array. And, the unified image formation scheme is implemented for SAR data processing. Then, the impulse response contour plot of the point target $P1$ are shown in Figure 11. Moreover, Table 3 demonstrates the quality measurement results of the point target $P1$, $P5$ and $P9$. Note that the rectangular window is used in azimuth.

Table 3. Point targets imaging qualities analysis.

target	Azimuth			Slant Range		
	ρ_a (m)	PSLR (dB)	ISLR (dB)	ρ_r (m)	PSLR (dB)	ISLR (dB)
			Stripmap mode			
$P1$	2.217	−13.222	−10.031	1.328	−13.260	−10.022
$P5$	2.217	−13.235	−10.030	1.329	−13.258	−10.022
$P9$	2.217	−13.231	−10.031	1.328	−13.261	−10.023
			Sliding spotlight			
$P1$	0.462	−13.257	−10.026	0.265	−13.266	−10.001
$P5$	0.459	−13.259	−10.030	0.266	−13.252	−10.001
$P9$	0.453	−13.257	−10.035	0.266	−13.250	−10.002
			Spotlight mode			
$P1$	0.174	−13.214	−10.040	0.133	−13.253	−10.002
$P5$	0.175	−13.232	−10.047	0.133	−13.222	−10.005
$P9$	0.175	−13.201	−10.030	0.133	−13.271	−10.000
			Inverse TOPS mode			
$P1$	11.788	−13.240	−10.003	5.316	−13.253	−10.003
$P5$	11.830	−13.264	−10.001	5.316	−13.265	−10.004
$P9$	11.898	−13.241	−10.002	5.316	−13.261	−10.009
			TOPS mode			
$P1$	12.346	−13.252	−10.007	6.644	−13.247	−10.006
$P5$	12.367	−13.262	−10.005	6.643	−13.253	−10.007
$P9$	12.432	−13.234	−10.005	6.643	−13.251	−10.008
			ScanSAR mode			
$P1$	16.344	−13.257	−10.004	11.080	−13.255	−10.005
$P5$	16.369	−13.258	−10.003	11.081	−13.258	−10.003
$P9$	15.403	−13.261	−10.001	11.080	−13.256	−10.000

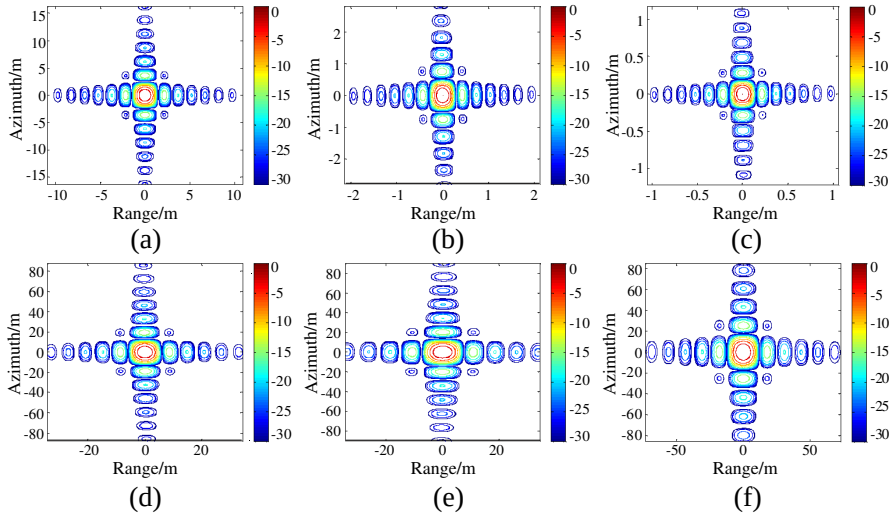

Figure 11. Contour plots of the point target $P1$ shows the processing results of (a) stripmap mode, (b) sliding spotlight mode, (c) spotlight mode, (d) inverse TOPS mode, (e) TOPS mode, and (f) ScanSAR mode.

According to the imaging qualities analysis of targets, we can find that multiple imaging modes of SAR data can be accurately processing by utilizing the proposed unified image formation scheme. And, the changes of azimuth resolution are also observed. Azimuth resolution of the point target at near slant range is better than the one at the far slant range in spotlight, inverse TOPS, TOPS and ScanSAR mode. However, opposite conclusion is obtained for sliding spotlight mode. Moreover, azimuth resolution is almost changeless in stripmap mode.

5. CONCLUSIONS

This paper proposed a novel unified image formation scheme for spaceborne SAR data processing. All spaceborne SAR imaging modes were quantitatively described by introducing a new parameter, i.e., UMC, basing on theoretical analysis together with SAR imaging geometry and time-frequency diagram.

A novel unified three-step image formation scheme is developed using UMC. The first step is to compensate extension of Doppler bandwidth effect result from azimuth antenna-beam steering. The second step implements azimuth and range focusing procedure. And, the third step removes image aliasing effects by means of re-sampling

operation. Consequently, all of SAR image formation procedures can be merged into a standard three-step processing framework, by which spaceborne SAR data processing is greatly simplified. As a result, the efficiency and robustness of data processing sub-system at SAR ground segment could be significantly improved.

UMC is defined as a one-dimension parameter in this paper. However, there would be new SAR modes being undergoing development, which may have different steering rules of range antenna-beam (e.g., azimuth + range steering). If the new imaging modes cannot be described by the UMC defined in the manuscript, a refined two-dimensional UMC should be studied for describing both azimuth and range steering rules of antenna-beam. And, this problem will be studied in our future work.

ACKNOWLEDGMENT

This work was supported by the National Natural Science Foundation of China (NSFC) under Grant No. 61132006 and No. 61171123.

REFERENCES

1. Ren, S., W. Chang, T. Jin, and Z. Wang, "Automated SAR reference image preparation for navigation," *Progress In Electromagnetics Research*, Vol. 121, 535–555, 2011.
2. Xu, W., P. P. Huang, and Y.-K. Deng, "Multi-channel SPCMB-TOPS SAR for high-resolution wide-swath imaging," *Progress In Electromagnetics Research*, Vol. 116, 533–551, 2011.
3. Tian, B., D.-Y. Zhu, and Z.-D. Zhu, "A novel moving target detection approach for dual-channel SAR system," *Progress In Electromagnetics Research*, Vol. 115, 191–206, 2011.
4. Storvold, R., E. Malnes, and Y. Larsen, "SAR remote sensing of snow parameters in Norwegian areas-current status and future perspective," *Journal of Electromagnetic Waves and Applications*, Vol. 20, No. 13, 1751–1759, 2006.
5. Chang, Y.-L., C.-Y. Chiang, and K.-S. Chen, "SAR image simulation with application to target recognition," *Progress In Electromagnetics Research*, Vol. 119, 35–57, 2011.
6. Zan, F. D. and A. M. Guarnieri, "TOPSAR: Terrain observation by progressive scans," *IEEE Trans. on Geosci. Remote Sens.*, Vol. 44, No. 9, 2352–2360, 2006.
7. Xu, W., P. P. Huang, and Y.-K. Deng, "MIMO-Tops mode

for high-resolution ultra-wide-swath full polarimetric imaging," *Progress In Electromagnetics Research*, Vol. 121, 19–37, 2011.

8. Ren, X. Z., Y. Qin, and L. H. Qiao, "Interferometric properties and processing for spaceborne spotlight SAR," *Progress In Electromagnetics Research B*, Vol. 36, 267–281, 2012.
9. Chan, Y. K., V. C. Koo, B. K. Chung, and H. T. Chuah, "Modified algorithm for real time SAR signal processing," *Progress In Electromagnetics Research C*, Vol. 1, 156–168, 2008.
10. Bamler, R. and M. Eineder, "ScanSAR processing using standard high precision SAR algorithm," *IEEE Trans. on Geosci. Remote Sens.*, Vol. 114, 17–32, 2011.
11. Wang, X. and D. Y. Zhu, "Range Doppler algorithm for bistatic SAR processing based on the improved loffeld's bistatic formula," *Progress In Electromagnetics Research Letter*, Vol. 21, 161–169, 2011.
12. Raney, R. K., H. Runge, and R. Bamler, "Precision SAR processing using chirp scaling," *IEEE Trans. on Geosci. Remote Sens.*, Vol. 32, No. 4, 786–799, 1994.
13. Moreira, A., J. Mittermayer, and R. Scheiber, "Extended chirp scaling algorithm for air- and spaceborne SAR data processing in stripmap and scanSAR imaging modes," *IEEE Trans. on Geosci. Remote Sens.*, Vol. 34, No. 5, 1123–1136, 1996.
14. Zhu, D., M. Shen, and Z. Zhu, "Some aspects of improving the frequency scaling algorithm for dechirped SAR data processing," *IEEE Trans. on Geosci. Remote Sens.*, Vol. 46, No. 6, 1579–1588, 2008.
15. Liu, Q., W. Hong, W. Tan, Y. Lin, Y. P. Wang, and Y. Wu, "An improved polar format algorithm with performance analysis for geosynchronous circular SAR 2D imaging," *Progress In Electromagnetics Research*, Vol. 119, 155–170, 2011.
16. Guo, D., H. Xu, and J. Li, "Extended wavenumber domain algorithm for highly squinted sliding spotlight SAR data processing," *Progress In Electromagnetics Research*, Vol. 114, 17–32, 2011.
17. Park, S.-H., J.-I. Park, and K.-T. Kim, "Motion compensation for squint mode spotlight SAR imaging using efficient 2D interpolation," *Progress In Electromagnetics Research*, Vol. 128, 503–518, 2012.
18. Mao, X., D.-Y. Zhu, and Z.-D. Zhu, "Signatures of moving target in polar format spotlight SAR image," *Progress In Electromagnetics Research*, Vol. 92, 47–64, 2009.

19. Chen, J., J. H. Gao, Y. Q. Zhu, W. Yang, and P. B. Wang, "A novel image formation algorithm for high-resolution wide-swath spaceborne SAR using compressed sensing on azimuth displacement phase center antenna," *Progress In Electromagnetics Research*, Vol. 125, 527–542, 2012.
20. An, D. X., Z.-M. Zhou, X.-T Huang, and T. Jin, "A novel imaging approach for high resolution squinted spotlight SAR based on the deramping-based technique and azimuth NLCS principle," *Progress In Electromagnetics Research*, Vol. 123, 485–508, 2012.
21. Lanari, R., S. Zoffoli, E. Sansosti, G. Fornaro, and F. Serafino, "New approach for hybrid strip-map/spotlight SAR data focusing," *IEE Proc. — Radar, Sonar, Navig.*, Vol. 148, No. 6, 363–372, 2001.
22. Prats, P., R. Scheiber, J. Mittermayer, A. Meta, and A. Moreira, "Processing of sliding spotlight and TOPS SAR data using baseband azimuth scaling," *IEEE Trans. on Geosci. Remote Sens.*, Vol. 48, No. 2, 770–780, 2010.
23. Yang, W., C. S. Li, J. Chen, and P. B. Wang, "Extend three-step focusing algorithm for sliding spotlight and TOPS data image formation," *IEEE International Geoscience and Remote Sensing Symposium (IGARSS)*, 479–482, 2011.
24. Belcher, D. P., and C. J. Baker, "High resolution processing of hybrid strip-map/spotlight mode SAR," *IEE Proc. — Radar, Sonar Navig.*, Vol. 143, No. 6, 366–374, 1996.
25. Cheng, H., T. Long, and Y. Tian "An improved nonlinear chirp scaling algorithm based on curved trajectory in geosynchronous SAR," *Progress In Electromagnetics Research*, Vol. 135, 481–513, 2013.
26. Mittermayer, J., S. Wollstadt, P. Prats, R. Scheiber, and W. Koppe, "Staring spotlight imaging with TerraSAR-X," *IEEE International Geoscience and Remote Sensing Symposium (IGARSS)*, 1606–1608, 2012.